Joint Adaptive AoA and Polarization Estimation Using Hybrid Dual-Polarized Antenna Arrays

Hang Li, Thomas Q. Wang, and Xiaojing Huang *Senior Member, IEEE*

***Abstract*—The propagation of a millimeter wave (mmWave) signal is dominated by its line-of-sight component. Therefore, the knowledge of angle-of-arrival and polarization state of the wave is of great importance for its reception at the receiver. In this paper, we estimate these parameters for an information-bearing signal in mmWave systems using hybrid antenna arrays with dual-polarized dipoles. The estimation is studied in the context of both the interleaved and localized arrays. Two blind adaptive algorithms, namely, the joint differential beam tracking and cross-correlation-to-power ratio polarization tracking, and the differential beam and polarization search, are developed, each tailored for an array. It is shown that the use of dual-polarized dipoles in combination with the developed algorithms effectively lead to polarization diversity which significantly enhances the signal-to-noise ratio at the decoder. The simulation results also show that the antennas with dual dipoles provide improved accuracy and convergence rate for the estimations compared with the conventional arrays.**

***Index Terms*—Hybrid dual-polarized antenna array, crossed dipoles, subarray, beamforming, angle-of-arrival estimation, polarization state estimation, and mmWave communications.**

I. Introduction

Millimetre wave (mmWave) communication is one of the most promising technologies for future wireless services. Thanks to the large spectrum ranging from 30 GHz to 300 GHz, mmWave communication has potentially enabled extremely high data rate which is unprecedented in conventional radio frequency (RF) systems. In addition, the vast spectrum is an effective supplement to augment the currently saturated RF bands (700 MHz to 2.6 GHz) for wireless communications. As a result, a large number of applications, e.g., 5G cellular systems, wireless local area networks and ad hoc networks, have been investigated using the mmWave [1]–[3].

The short wavelength of mmWave enables the use of massive antenna arrays in the transceivers to overcome the path loss and to provide beamforming and spatial multiplexing. The arrays can be configured in a number of architectures which reflect the trade-offs between the performance and the costs of hardware implementation, power consumption and real-time signal processing. The fully digital array is a performance-orientated architecture in which each antenna is connected to a dedicated RF chain. It is seamlessly compatible with the classic multiple-input multiple-output (MIMO) technologies and thus leads to the best performance in terms of data rate. However, the implementation of a fully digital array involves prohibitive costs, particularly for a large array. Alternatively, hybrid architectures can be employed in the array to reduce the associated costs. In these architectures, analog beamformers (phase shifters) are used to connect the RF chains with antennas and to adjust the directivity of the array. Depending on the connection, a hybrid array can be configured to be fully- or partially-connected. A fully-connected array is known for the total connections between each of its RF chains and all the antenna elements. It provides narrow beams for its RF chains and thus leads to sub-optimal data rate [4]. The challenge of implementing fully-connected arrays stems from the dimensions and power consumption demanded by an enormous amount of phase shifters. The hybrid partially-connected array is a practical solution for the transceivers [5], [6]. Unlike its fully-connected counterpart, each RF chain in a partially-connected array is connected to a subset of elements (subarray) only. This is more suitable for hardware and physical deployment with massive array, and thus makes it a topic increasingly studied in recent years. A partially-connected array can be categorized into two types of regular configurations according to the topology of subarrays, i.e., interleaved and localized arrays. They have different characteristics and satisfy different demands [5]. The interleaved array provides narrower beam width, while the localized array generates smaller side lobes. Therefore, the former is more applicable to generating multi-beam for space division multiple access, while the latter is preferred to support systems with larger angle-of-arrival (AoA) range. From the view of hardware implementation, the localized array is easier to assemble multiple modules to form a large array in feeding networks.

The channel of mmWave is characterized by limited scattering and diminished diffraction in multipath environments [5]. Therefore, the line-of-sight (LOS) propagation typically dominates when a wave reaches its destination, leading to the received wave having dominant polarization and AoA over those of non-LOS (NLOS) conditions. There has been extensive research on massive array with single-polarized antennas for receiving incident waves [2], [4], [5], where the effect caused by polarization mismatch is not considered. These antennas are able to collect sufficient power of a wave from the ubiquitous scatters in RF bands, but cannot be directly used in mmWave due to the possible mismatch

This work was supported in part by Australian Research Council Discovery Project DP160101693, and in part by MEXT-Japan, KAKENHI, Fund for the Promotion of Joint International Research, Fostering Joint International Research (B) (18KK0277).

H. Li is now with the College of Electronics and Information, Hangzhou Dianzi University, Hangzhou, China. He was with the Global Big Data Technologies Centre, University of Technology Sydney, Sydney, Australia (Email: hanglidsp@gmail.com).

T. Q. Wang and X. Huang are with the Global Big Data Technologies Centre, University of Technology Sydney, Sydney, Australia (Emails: {Qian.Wang, Xiaojing.Huang}@uts.edu.au).

between the (dominant) polarization direction of the wave and that of the antennas. The antennas can only receive the component of an electric field projected onto them and will miss that perpendicular to them. Alternatively, dual-polarized antennas with crossed dipoles can be employed to enhance the reception for both sub-6 GHz and mmWave systems [7]–[9], whereas there are differences in subsequent signal processing methods between both systems due to different array structures adopted. The use of dual dipoles enables the received signal to have the vertical and horizontal components of the electric field, each received by a dipole. As a result, compared with its single-polarized counterpart, the dual-polarized antennas ensure more power received and provide more dimensions for digital signal processing. Recent works in [10], [11] have studied the beam alignment and selection algorithms for dual-polarized mmWave MIMO systems, respectively. Simulation results have shown that better system performance is achieved by exploiting polarization diversity.

The knowledge of AoA and polarization state of an incident wave is of great importance for its reception by a massive array. It can facilitate the beam alignment and the combination of polarization diversity between the transmitter and the receiver, and thus enhance the signal-to-noise ratio (SNR) at the decoder. The existing hybrid arrays employing single-dipole antenna elements can only perform AoA estimation. Depending on the architecture, different methods have been developed for fully- and partially-connected arrays. In [12], adaptive compressed sensing (CS) technique is exploited to estimate the AoA of mmWave signals for fully-connected arrays, whereas the work in [13] applies the classic methods of MUltiple SIgnal Classification (MUSIC) [14] and Estimation of Signal Parameters via Rotational Invariance Techniques (ESPRIT) [15] to partially-connected arrays. Although they potentially provide outstanding performance, the prohibitive computational complexity prevents them from being applied in massive arrays. With the designed efficient multi-resolution codebook, the work in [16] enables hierarchical search method to be performed to rapidly find one single multipath component (MPC) and thus the AoA. Furthermore in [17], a CS based approach is proposed to recover multiple real MPCs by exploiting the sparse nature of mmWave channel. Such codebook based methods require the transmitter repeatedly to narrow down the beam. This will introduce the extra overhead and the estimation accuracy is subject to the resolutions of the codebooks. The use of multiple subarrays means that the signals received by adjacent subarrays have a constant phase difference which depends on the AoA. In light of this, the estimation using partially-connected arrays is equivalent to evaluating this difference. In [18] and [19], the evaluation is accomplished by adaptive filtering, which is then improved in [20]–[22] for better accuracy and convergence speed.

Fully digital arrays with crossed dipoles have been extensively studied to estimate the AoA and polarization state [23]–[25]. The estimation is conducted by using ESPRIT in which the computations of the covariance matrix and singular value decomposition (SVD) are performed to extract the AoA and polarization state information. As the size of the arrays increases, the computational complexity of SVD grows cubically with the total number of antennas [21], resulting in the impractically high cost of implementation. Therefore, the developed techniques can be only applied to the arrays with modest sizes.

In this paper, we study hybrid partially-connected massive arrays using dual-polarized antennas to enhance the reception of an information-bearing mmWave signal. The estimation methods of AoA and polarization state are studied for two typical partially-connected arrays, i.e., the interleaved and localized arrays [18]. We show that the new methods lead to polarization diversity which coherently combines the signals from the dual-dipoles to produce enhanced SNR. The contributions also include

- For the dual-polarized interleaved arrays, we develop a joint differential beam tracking (DBT) and cross-correlation-to-power ratio polarization tracking (CPRPT) estimation algorithm to effectively estimate AoA and polarization state. Unlike those based on subspace-based methods, e.g., ESPRIT and MUSIC, the proposed algorithm is a cross-correlation based approach in which scalar (complex) multiplications and additions only are involved. Therefore, its complexity is much less than the existing ones. Also, the algorithm is blind adaptive and Doppler resilient.
- To remove the phase ambiguity in the dual-polarized localized arrays, we further develop a differential beam and polarization search (DBPS) estimation algorithm, in which the real phase can be identified based on the estimated signal power.
- We formulate the polarization state estimation as the problem of estimating the ratio of cross-correlation to power of the beamformed signal in the presence of recursive nuisance parameters. Upper bounds of the average SNRs are derived, showing that the proposed estimator is asymptotically unbiased. Numerical and simulation results show that our proposed algorithms are able to dramatically reduce the mean square error (MSE) through a number of iterations.

The remainder of this paper is organized as follows. Section II introduces the planar hybrid dual-polarized interleaved and localized arrays, and describes the received signal models. Section III and IV propose a joint DBT and CPRPT estimation algorithm, and a DBPS estimation algorithm for both interleaved and localized arrays, respectively. Section V evaluates the performance of the proposed polarization estimation. In Section VI, numerical and simulation results are given to demonstrate the performance of the proposed estimation algorithms, before concluding the paper in Section VII.

II. System Models

A. Partially-Connected Array with Crossed-Dipole Antennas

A partially-connected array typically consists of several subarrays of antenna elements. Depending on the grouping of the elements, an array can be configured as an interleaved or localized array [18]. Fig. 1 illustrates these configurations using a uniform planar array (UPA). As shown in the figure, the

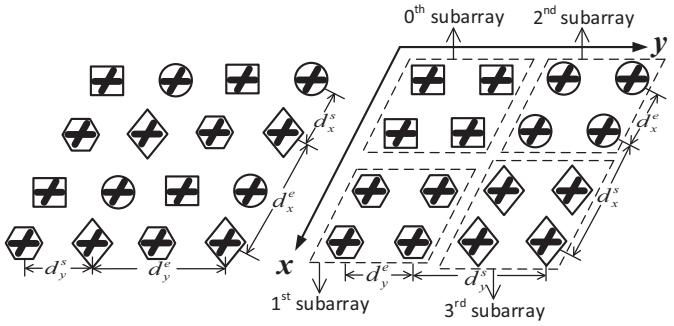

Fig. 1. Two-by-two planar dual-polarized interleaved array (left) versus localized array (right). Each antenna element includes two crossed dipoles. The profile shape of each element indicates the subarray to which it belongs.

interleaved array has subarrays with the elements distributed in a scattered manner over the whole array, whereas the localized array puts together neighbouring elements to form subarrays. Denote the intervals between neighbouring subarrays in x- and y-directions by d_x^s and d_y^s, and those between neighbouring elements by d_x^e and d_y^e. Then the intervals are given by $d_x^s = d_y^s = d$, $d_x^e = M_x d$ and $d_y^e = M_y d$ for interleaved arrays, and by $d_x^e = d_y^e = d$, $d_x^s = N_x d$ and $d_y^s = N_y d$ for localized arrays. Here d denotes the spacing between adjacent elements in the array, M_x and M_y, the numbers of subarrays in x- and y-directions, and N_x and N_y, the numbers of elements in a subarray in the two directions.

In line with the enormous research on the signal processing techniques for massive antenna arrays, the considered arrays are assumed to employ antenna elements with omnidirectional radiation patterns [5], [20], [21]. Each element has two spatially collocated orthogonal dipoles [26], denoted by x-axis and y-axis dipoles, respectively, which without loss of generality are assumed along the x- and y-directions respectively. The dipoles are used to measure the components of the incoming electric field projected onto the directions of x- and y-axes. Therefore, an incident wave can simultaneously stimulate two signals in an antenna, each from a dipole. Accordingly, in an array, two sets of signals collected from all the x- and y-axis dipoles respectively can be formed. From the perspective of signal reception, they represent two replicas of the signal (wave), which can be coherently combined to enhance the SNR at the decoder. The diversity combining depends on the individual SNRs of each dipole, and thus requires their estimates which can be obtained through the estimations of AoA and polarization state of the incident wave.

The reception of the wave using a two-by-two dual-polarized localized array and the associated signal processing modules are illustrated in Fig. 2, where the RF and down conversion components are omitted for simplicity. The replicas are processed separately and identically in analog and digital domains for the estimations of AoA and polarization state. The modules for x- and y-axis dipoles are included in the figure, with those for x-axis dipoles elaborated in the red and blue dashed boxes and y-axis dipoles enclosed in the corresponding solid ones. Although the numbers of analog and digital beamformers are doubled, they are the necessary components for polarization estimation and coherent combination.

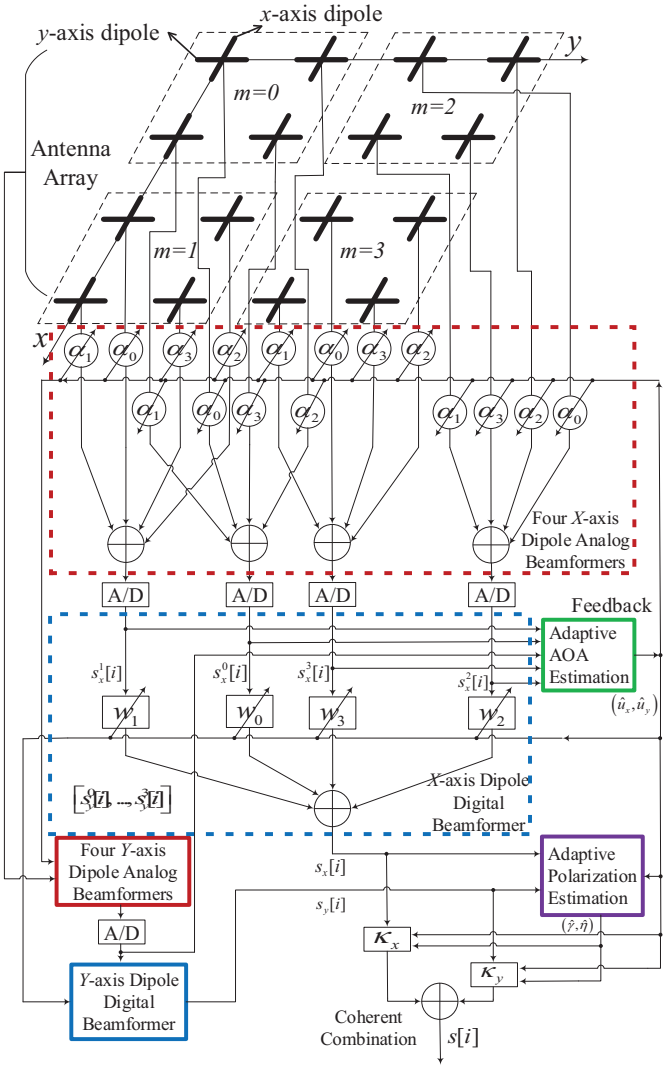

Fig. 2. Illustration of two-by-two dual-polarized localized array.

B. Received Signal Model

We consider the reception of a narrow-band[1] plane-wave reference signal $\tilde{s}(t)$ using a UPA consisting of $M_x \times M_y$ subarrays. Identical phase shifts are assumed in all the subarrays, i.e., for any given subarray, its phase shifts are given by $\alpha_0, ..., \alpha_{N_x N_y - 1}$, where the product, $N_x N_y$ denotes the number of elements in a subarray. The signal with an unknown polarization state and AoA is assumed to have a carrier wavelength of λ, subject to a Doppler frequency shift, f_D. Ignoring the mutual couplings between elements[2] [18] and between the dual dipoles in an element[3] [27], the received signals at the

[1]The proposed estimation methods can be potentially extended to wideband mmWave systems, where the proposed ones are applied to all subcarriers and frequency-domain AoA estimation [19] and polarization estimation can be performed.

[2]The mutual coupling effect between different antenna elements can be considered as a distortion of the subarray radiation pattern, leading to a degraded SNR in our model. This will deteriorate the estimation performance determined by the SNR. However, as reported in [19], the MSE achieved by the adaptive algorithm in an environment without mutual coupling can be also achieved by the same algorithm in a mutual coupling environment with more iterations.

[3]In the literature studying the signal processing techniques for dual-polarized arrays [23]–[25], [27], ignoring mutual coupling effect between two dipoles is typically assumed.

output of the mth analog beamformer ($m = m_y M_x + m_x$; $m_x = 0, ..., M_x - 1$; $m_y = 0, ..., M_y - 1$) can be expressed as

$$\begin{aligned}[s_x^m(t), s_y^m(t)] =& \frac{[E_x, E_y]}{\sqrt{|E_x|^2 + |E_y|^2}} \tilde{s}(t) e^{j2\pi f_D t} P_s(\theta, \phi) \\ & \cdot e^{j\frac{2\pi}{\lambda}(m_x d_x^s \sin\theta\cos\phi + m_y d_y^s \sin\theta\sin\phi)} \\ & + [\xi_x^m(t), \xi_y^m(t)], \end{aligned} \tag{1}$$

where

$$\begin{aligned} E_x =& \sin\gamma\cos\theta\cos\phi e^{j\eta} - \cos\gamma\sin\phi \\ E_y =& \sin\gamma\cos\theta\sin\phi e^{j\eta} + \cos\gamma\cos\phi, \end{aligned} \tag{2}$$

denote the responses of *x*- and *y*-axis dipoles respectively, which are normalized in the form of $\frac{[E_x, E_y]}{\sqrt{|E_x|^2+|E_y|^2}}$. Note that in contrast to the signal model presented in [18] not studying the polarization, (1) considers the components of the electric field projected onto the directions of *x*- and *y*-axes, which can be used to estimate the polarization state and thus improve the SNR with coherent diversity combining. $(\theta, \phi) \in [-\frac{\pi}{2}, \frac{\pi}{2})$ denote the AoA in terms of the incident signal's zenith and azimuth angles, respectively. $\gamma \in [0, \frac{\pi}{2})$ represents the auxiliary polarization angle and $\eta \in [-\pi, \pi)$ represents the polarization phase difference [27], which uniquely determine the polarization state of a wave. For example, $\eta = 0$ refers to linearly-polarized waves, while $\gamma = \frac{\pi}{4}$ and $\eta = \pm\frac{\pi}{2}$ refer to left/right circularly-polarized wave. $\xi_x^m(t)$ and $\xi_y^m(t)$ are the complex additive white Gaussian noises (AWGNs) corresponding to the *x*- and *y*-axis dipoles at the outputs of the mth subarray. $P_s(\theta, \phi)$ denotes the normalized subarray radiation pattern, and when the phase shift of the nth element ($n = n_y N_x + n_x$; $n_x = 0, ..., N_x - 1$; $n_y = 0, ..., N_y - 1$) in a subarray is chosen as $\alpha_n = -\frac{2\pi}{\lambda}(n_x d_x^e \sin\theta'\cos\phi' + n_y d_y^e \sin\theta'\sin\phi')$, it can be written as

$$\begin{aligned} P_s(\theta, \phi) =& \frac{1}{N_x N_y} \sum_{n_y=0}^{N_y-1} \sum_{n_x=0}^{N_x-1} e^{j\left[\frac{2\pi}{\lambda}(n_x d_x^e \sin\theta\cos\phi \right.} \\ & \left. + n_y d_y^e \sin\theta\sin\phi) + \alpha_n\right] \\ =& \frac{\sin\left[N_x \frac{\pi}{\lambda} d_x^e (\sin\theta\cos\phi - \sin\theta'\cos\phi')\right]}{N_x \sin\left[\frac{\pi}{\lambda} d_x^e (\sin\theta\cos\phi - \sin\theta'\cos\phi')\right]} \\ & \cdot \frac{\sin\left[N_y \frac{\pi}{\lambda} d_y^e (\sin\theta\sin\phi - \sin\theta'\sin\phi')\right]}{N_y \sin\left[\frac{\pi}{\lambda} d_y^e (\sin\theta\sin\phi - \sin\theta'\sin\phi')\right]}, \end{aligned} \tag{3}$$

which has the subarray main beam directed towards the direction/AoA represented by the angles (θ', ϕ').

The outputs of the beamformers are then converted into digital signals via analog-to-digital (A/D) converters. The samples sampled at the iTth instance are denoted by $[s_x^m[i], s_y^m[i]] = [s_x^m(iT), s_y^m(iT)]$, where T represents the sampling interval which equals the width of a symbol carried by the wave. As shown in Fig. 2, these samples are used to estimate the AoA and to update the phase shifters accordingly. The samples from *x*- and *y*-axis dipoles are weighted and summed separately by digital beamformers as

$$[s_x[i], s_y[i]] = \sum_{m=0}^{M_x M_y - 1} w_m \left[s_x^m[i], s_y^m[i]\right], \tag{4}$$

where $\omega_0, ..., \omega_{M_x M_y - 1}$ denote the coefficients which align the phases of the samples. The resulting samples, $[s_x[i], s_y[i]]$, each from a dipole, are used to estimate the polarization state and also for maximal ratio combining (MRC) which produces a combined sample, $s[i]$, with polarization diversity. The sample can be expressed as

$$s[i] = [\kappa_x, \kappa_y] [s_x[i], s_y[i]]^T = \kappa_x s_x[i] + \kappa_y s_y[i], \tag{5}$$

where $[\kappa_x, \kappa_y]$ are the MRC coefficients, and $[\cdot]^T$ denotes the transpose. It can be seen from (1) that the coefficients depend on both the AoA and polarization state which can be estimated using the proposed array.

III. Joint Adaptive AoA and Polarization Estimation for Interleaved Arrays

In this section, we consider the reception of the wave using an interleaved array. In order to produce the maximum SNR at the decoder, the array calibrates its analog and digital beamformers and the MRC coefficients through the estimations of AoA and polarization state. The estimations are given by an iterative procedure, where in each iteration the AoA and polarization state are estimated based on the current and previous samples.

A. Differential Beam Tracking for AoA Estimation

The reception using an interleaved array leads to the outputs of the neighbouring subarrays, $\left[s_x^m(t), s_y^m(t)\right]$ and $\left[s_x^{m+1}(t), s_y^{m+1}(t)\right]$, having a constant phase difference which depends on the AoA of the wave [18]. This holds as long as $P_s(\theta, \phi)$ is nonzero. Therefore, an estimate of AoA can be evaluated by extracting the phase of the cross-correlation of the outputs. This is known as the DBT. We denote the cross-correlations between two adjacent subarrays in *x*- and *y*-directions by $[R_{xx}, R_{yx}]$ and $[R_{xy}, R_{yy}]$, respectively. Assuming the noise components to be independent, we have

$$\begin{aligned}[R_{xx}, R_{yx}] =& [\mathbb{E}[(s_x^m(t))^* s_x^{m+1}(t)], \mathbb{E}[(s_y^m(t))^* s_y^{m+1}(t)]] \\ =& \frac{[|E_x|^2, |E_y|^2]}{|E_x|^2 + |E_y|^2} \mathbb{E}[|\tilde{s}(t)|^2] |P_s(\theta, \phi)|^2 e^{ju_x} \end{aligned} \tag{6}$$

and

$$\begin{aligned}[R_{xy}, R_{yy}] =& [\mathbb{E}[(s_x^m(t))^* s_x^{m+M_x}(t)], \mathbb{E}[(s_y^m(t))^* s_y^{m+M_x}(t)]] \\ =& \frac{[|E_x|^2, |E_y|^2]}{|E_x|^2 + |E_y|^2} \mathbb{E}[|\tilde{s}(t)|^2] |P_s(\theta, \phi)|^2 e^{ju_y}, \end{aligned} \tag{7}$$

where

$$\begin{aligned} u_x =& \frac{2\pi}{\lambda} d_x^s \sin\theta\cos\phi \\ u_y =& \frac{2\pi}{\lambda} d_y^s \sin\theta\sin\phi, \end{aligned} \tag{8}$$

and $(\cdot)^*$, $\mathbb{E}[\cdot]$ and $|(\cdot)|$ represent the conjugate, expectation and absolute value of $(\cdot)$, respectively. It can be seen that the AoA is included in u_x and u_y which are in the range $[-\pi, \pi)$ given $d_x^s = d_y^s = d$ with $d \leq \frac{\lambda}{2}$. In addition, R_{xx} and R_{yx} have an identical phase, u_x, and R_{xy} and R_{yy}, u_y. Therefore, the sums, $R_{xx} + R_{yx}$ denoted by R_x, and $R_{xy} + R_{yy}$ denoted by R_y, have their individual components added in phase,

$$\hat{R}_x^{(i)} = (1-\mu_a)\hat{R}_x^{(i-1)} + \mu_a \sum_{m_y=0}^{M_y-1}\sum_{m_x=0}^{M_x-2}\left[(s_x^{m_yM_x+m_x}[i])^* s_x^{m_yM_x+m_x+1}[i] + (s_y^{m_yM_x+m_x}[i])^* s_y^{m_yM_x+m_x+1}[i]\right]$$
$$\hat{R}_y^{(i)} = (1-\mu_a)\hat{R}_y^{(i-1)} + \mu_a \sum_{m_x=0}^{M_x-1}\sum_{m_y=0}^{M_y-2}\left[(s_x^{m_yM_x+m_x}[i])^* s_x^{(m_y+1)M_x+m_x}[i] + (s_y^{m_yM_x+m_x}[i])^* s_y^{(m_y+1)M_x+m_x}[i]\right]. \quad (9)$$

leading to $u_x = \arg\{R_x\}$ and $u_y = \arg\{R_y\}$, respectively. Here $\arg\{\cdot\}$ denotes the argument of a complex number, falling in the range $[-\pi, \pi)$. The estimates of (θ, ϕ) can be determined by using the extracted phases, u_x and u_y, given by $\theta = \text{sign}\{u_x\}\arcsin\left(\frac{\lambda\sqrt{u_x^2+u_y^2}}{2\pi d}\right)$ and $\phi = \arctan\left(\frac{u_y}{u_x}\right)$, where $\text{sign}\{\cdot\}$ takes the sign of $\{\cdot\}$.

The estimation is implemented in digital domain where the continuous signal waveforms, $\left[s_x^m(t), s_y^m(t)\right]$ and $\left[s_x^{m+1}(t), s_y^{m+1}(t)\right]$, are converted to samples, $\left[s_x^m[i], s_y^m[i]\right]$ and $\left[s_x^{m+1}[i], s_y^{m+1}[i]\right]$. Also, the expectation with respect to the statistics of the signals given by (6) and (7) is approximated by a weighted sum of the previous and instantaneous estimates. The correlation coefficients, R_x and R_y, are estimated and adjusted iteratively using the samples taken across time. Denote the estimates of the cross-correlations in *x*- and *y*-directions returned by the first $i-1$ iterations (samples) by $\hat{R}_x^{(i-1)}$ and $\hat{R}_y^{(i-1)}$, respectively. Taking into account the ith samples, the updates in the ith iteration can be expressed as (9), where $0 < \mu_a < 1$ is the updating coefficient. As shown in (9), the adjustment caused by the new samples in the ith iteration is given by the sum across all the neighbouring subarrays in *x*-/*y*-directions and dipoles. The resulting computation at the ith iteration needs $(M_x-1)M_y$ and $(M_y-1)M_x$ complex multiplications, and $(M_x-1)M_y+2$ and $(M_y-1)M_x+2$ additions for $\hat{R}_x^{(i)}$ and $\hat{R}_y^{(i)}$, respectively. As each (product) term has a phase of $u_x(u_y)$ in the absence of additive noise, the sum of them will constructively increase the signal component with the phase, $u_x(u_y)$. Therefore, this leads to faster convergence and higher accuracy for the tracking. Then, the analog and digital beamformers are adjusted accordingly to have the array align with the estimated u_x and u_y, i.e., $\hat{\alpha}_{n_yN_x+n_x}^{(i)} = -(n_xM_x\hat{u}_x^{(i-1)} + n_yM_y\hat{u}_y^{(i-1)})$ and $\hat{w}_{m_yM_x+m_x}^{(i)} = \frac{1}{M_xM_y}e^{-j(m_x\hat{u}_x^{(i)}+m_y\hat{u}_y^{(i)})}$, where $\hat{u}_x^{(i)} = \arg\{\hat{R}_x^{(i)}\}$ and $\hat{u}_y^{(i)} = \arg\{\hat{R}_y^{(i)}\}$.

B. Cross-correlation-to-power Ratio Polarization Tracking

As demonstrated in Fig. 2, the polarization state, (γ, η), is estimated based on the samples, $s_x[i]$ and $s_y[i]$, at the outputs of the digital beamformers of *x*- and *y*-axis dipoles. Using the updated weights of the beamformers, we can express the output samples as

$$\begin{aligned}&[s_x[i], s_y[i]]\\ &= \underbrace{\frac{[E_x, E_y]}{\sqrt{|E_x|^2+|E_y|^2}}\tilde{s}[i]e^{j2\pi f_D T i}P_s(\theta,\phi)P_c(u_x,u_y)}_{\textbf{\textit{signal components}}}\\ &\quad + \underbrace{\frac{1}{M_xM_y}\sum_{m_y=0}^{M_y-1}\sum_{m_x=0}^{M_x-1}[\xi_x^m[i], \xi_y^m[i]]e^{-j(m_x\hat{u}_x^{(i)}+m_y\hat{u}_y^{(i)})}}_{\textbf{\textit{noise components}}},\end{aligned} \quad (10)$$

where

$$\begin{aligned}&P_c(u_x,u_y)\\ &= \frac{1}{M_xM_y}\sum_{m_y=0}^{M_y-1}\sum_{m_x=0}^{M_x-1}e^{j[m_x(u_x-\hat{u}_x^{(i)})+m_y(u_y-\hat{u}_y^{(i)})]}\\ &= \frac{\sin\left[M_x(u_x-\hat{u}_x^{(i)})/2\right]}{M_x\sin\left[(u_x-\hat{u}_x^{(i)})/2\right]}\cdot\frac{\sin\left[M_y(u_y-\hat{u}_y^{(i)})/2\right]}{M_y\sin\left[(u_y-\hat{u}_y^{(i)})/2\right]},\end{aligned} \quad (11)$$

and $\tilde{s}[i] = \tilde{s}(iT)$ denotes the sample of the reference signal taken at the instance $t = iT$. Its power is given by $\sigma_{\tilde{s}}^2 = \mathbb{E}\left[|\tilde{s}[i]|^2\right]$. $[\xi_x^m[i], \xi_y^m[i]]$ are independent complex AWGNs at the outputs of the mth subarray with the same power σ_n^2.

As shown in (10), the polarization state, (γ, η), is contained in the normalized responses, $\frac{[E_x,E_y]}{\sqrt{|E_x|^2+|E_y|^2}}$, and thus can be extracted by exploiting their relative values. We employ the relative values given by the stochastic cross-correlation and powers of the signal components of (10) which, denoted by $[Q_{xy}, P_x, P_y]$, can be expressed as

$$\begin{aligned}&[Q_{xy}, P_x, P_y]\\ &= \frac{[E_xE_y^*, |E_x|^2, |E_y|^2]}{|E_x|^2+|E_y|^2}\sigma_{\tilde{s}}^2|P_s(\theta,\phi)|^2\left|P_c(u_x,u_y)\right|^2.\end{aligned} \quad (12)$$

Eq. (12) indicates that the polarization state included in E_x and E_y can be obtained through the ratios, Q_{xy}/P_x and Q_{xy}/P_y.

Given $[Q_{xy}, P_x, P_y]$, two cross-correlation-to-power ratios can be respectively expressed as

$$\begin{aligned}U_x + jV_x &= \frac{Q_{xy}}{P_x}\\ &= \frac{E_y^*}{E_x^*} = \frac{\sin\gamma\cos\theta\sin\phi e^{-j\eta} + \cos\gamma\cos\phi}{\sin\gamma\cos\theta\cos\phi e^{-j\eta} - \cos\gamma\sin\phi}\end{aligned} \quad (13)$$

and

$$U_y + jV_y = \frac{Q_{xy}}{P_y} = \frac{E_x}{E_y} = \frac{\sin\gamma\cos\theta\cos\phi e^{j\eta} - \cos\gamma\sin\phi}{\sin\gamma\cos\theta\sin\phi e^{j\eta} + \cos\gamma\cos\phi}, \quad (14)$$

which lead to the polarization state given by

$$\begin{cases} \gamma = \arctan\left\{\cos^{-1}\theta\sqrt{\dfrac{(U_x\tan\phi+1)^2 + V_x^2\tan^2\phi}{(U_x-\tan\phi)^2+V_x^2}}\right\} \\ \eta = \text{sign}\{\sin\eta\}\arccos(\cos\eta) \end{cases} \quad (15)$$

and

$$\begin{cases} \gamma = \arctan\left\{\cos^{-1}\theta\sqrt{\dfrac{(U_y\cot\phi+1)^2 + V_y^2\cot^2\phi}{(U_y-\cot\phi)^2+V_y^2}}\right\} \\ \eta = \text{sign}\{\sin\eta\}\arccos(\cos\eta), \end{cases} \quad (16)$$

respectively, where for (15)

$$\begin{aligned} \sin\eta =& \frac{V_x}{Y_x}\left(\sqrt{\frac{(U_x\tan\phi+1)^2+V_x^2\tan^2\phi}{(U_x-\tan\phi)^2+V_x^2}}\right. \\ & \left. - \tan^2\phi\sqrt{\frac{(U_x-\tan\phi)^2+V_x^2}{(U_x\tan\phi+1)^2+V_x^2\tan^2\phi}}\right) \\ \cos\eta =& Y_x^{-1}\left[(U_x-\tan\phi)\sqrt{\frac{(U_x\tan\phi+1)^2+V_x^2\tan^2\phi}{(U_x-\tan\phi)^2+V_x^2}}\right. \\ & \left. +\tan\phi(U_x\tan\phi+1)\sqrt{\frac{(U_x-\tan\phi)^2+V_x^2}{(U_x\tan\phi+1)^2+V_x^2\tan^2\phi}}\right] \\ Y_x =& 1+2U_x\tan\phi-\tan^2\phi, \end{aligned} \quad (17)$$

and for (16)

$$\begin{aligned} \sin\eta =& \frac{V_y}{Y_y}\left(\sqrt{\frac{(U_y\cot\phi+1)^2+V_y^2\cot^2\phi}{(U_y-\cot\phi)^2+V_y^2}}\right. \\ & \left. - \cot^2\phi\sqrt{\frac{(U_y-\cot\phi)^2+V_y^2}{(U_y\cot\phi+1)^2+V_y^2\cot^2\phi}}\right) \\ \cos\eta =& -Y_y^{-1}\left[(U_y-\cot\phi)\sqrt{\frac{(U_y\cot\phi+1)^2+V_y^2\cot^2\phi}{(U_y-\cot\phi)^2+V_y^2}}\right. \\ & \left. +\cot\phi(U_y\cot\phi+1)\sqrt{\frac{(U_y-\cot\phi)^2+V_y^2}{(U_y\cot\phi+1)^2+V_y^2\cot^2\phi}}\right] \\ Y_y =& 1+2U_y\cot\phi-\cot^2\phi, \end{aligned} \quad (18)$$

where $\cos\theta$ and $\tan\phi$ can be obtained from $\hat{u}_x$ and $\hat{u}_y$, as $\cos\theta = \sqrt{1-\left(\frac{\lambda}{2\pi d}\right)^2(\hat{u}_x^2+\hat{u}_y^2)}$ and $\tan\phi = \hat{u}_y/\hat{u}_x$. See Appendix A for the derivation of (15)-(18).

The basic principle of the CPRPT algorithm is to compute the polarization state by exploiting the ratios given by (13) and (14). As the AoA estimation proceeds, the directivity of array will be gradually adjusted to the real AoA, leading to increasing powers of the signal components in both x- and y-axis dipoles. In addition, the increase of signal power also results in increasing SNR for the cross-correlation (See Section V for details). As a result, it can be seen that the accuracy of the estimation improves as the iteration proceeds.

TABLE I
THE JOINT DBT AND CPRPT ALGORITHM

Initialization: $\hat{u}_x^{(0)}$, $\hat{u}_y^{(0)}$, $\hat{R}_x^{(0)}$, $\hat{R}_y^{(0)}$, $\hat{Q}_{xy}^{(0)}$, $\hat{P}_x^{(0)}$and $\hat{P}_y^{(0)}$;

For $i = 1 : I_1$ (I_1 is the number of iterations.)

1. Set $\hat{\alpha}^{(i)}_{n_yN_x+n_x} = -(n_xM_x\hat{u}_x^{(i-1)} + n_yM_y\hat{u}_y^{(i-1)})$, $n_x = 0, ..., N_x-1, n_y = 0, ..., N_y-1$;
2. Update $[s_x^m[i], s_y^m[i]]$ using $\hat{\alpha}^{(i)}_{n_yN_x+n_x}$ in (1);
3. Update $\hat{R}_x^{(i)}$ and $\hat{R}_y^{(i)}$ using (9);
4. Calculate $\hat{u}_x^{(i)} = \arg\{\hat{R}_x^{(i)}\}$ and $\hat{u}_y^{(i)} = \arg\{\hat{R}_y^{(i)}\}$;
5. Update $\hat{w}^{(i)}_{m_yM_x+m_x} = \frac{1}{M_xM_y}e^{-j(m_x\hat{u}_x^{(i)}+m_y\hat{u}_y^{(i)})}$, $m_x = 0, ..., M_x-1$, $m_y = 0, ..., M_y-1$;
6. Update $[s_x[i], s_y[i]]$ using $\hat{w}^{(i)}_{m_yM_x+m_x}$ in (10);
7. Update $\left[\hat{Q}_{xy}^{(i)}, \hat{P}_x^{(i)}, \hat{P}_y^{(i)}\right]$ using (19);
8. Determine $\hat{\gamma}^{(i)}$ and $\hat{\eta}^{(i)}$ using (15) or (16);
9. Determine $\hat{\kappa}_x^{(i)}$ and $\hat{\kappa}_y^{(i)}$ using (20).

End for

In the presence of additive noise, $[Q_{xy}, P_x, P_y]$ are estimated by using the outputs of the digital beamformers. In line with the AoA estimation, they are evaluated iteratively, with the values derived by the ith iteration, $\left[\hat{Q}_{xy}^{(i)}, \hat{P}_x^{(i)}, \hat{P}_y^{(i)}\right]$, related to those by the $(i-1)$th iteration, $\left[\hat{Q}_{xy}^{(i-1)}, \hat{P}_x^{(i-1)}, \hat{P}_y^{(i-1)}\right]$, by

$$\begin{aligned} & \left[\hat{Q}_{xy}^{(i)}, \hat{P}_x^{(i)}, \hat{P}_y^{(i)}\right] \\ =& (1-\mu_p)\left[\hat{Q}_{xy}^{(i-1)}, \hat{P}_x^{(i-1)}, \hat{P}_y^{(i-1)}\right] \\ & + \mu_p\left[s_x[i]s_y^*[i], |s_x[i]|^2 - \frac{\sigma_n^2}{M_xM_y}, |s_y[i]|^2 - \frac{\sigma_n^2}{M_xM_y}\right], \end{aligned} \quad (19)$$

where $0 < \mu_p < 1$ is the updating coefficient, and $\sigma_n^2/(M_xM_y)$ is the power of noise component in (10). It can be seen that $M_x + M_y + 3$ complex multiplications and $M_x + M_y + 1$ additions are required to form $\left[\hat{Q}_{xy}^{(i)}, \hat{P}_x^{(i)}, \hat{P}_y^{(i)}\right]$ at the ith iteration. Then the MRC coefficients, $[\hat{\kappa}_x^{(i)}, \hat{\kappa}_y^{(i)}] = [\hat{\nu}_x^{(i)}, \hat{\nu}_y^{(i)}]/\sqrt{|\hat{\nu}_x^{(i)}|^2 + |\hat{\nu}_y^{(i)}|^2}$, can be obtained accordingly by

$$\begin{aligned} \hat{\nu}_x^{(i)} =& \sin\hat{\gamma}^{(i)}\cos\hat{\theta}^{(i)}\cos\hat{\phi}^{(i)}e^{-j\hat{\eta}^{(i)}} - \cos\hat{\gamma}^{(i)}\sin\hat{\phi}^{(i)} \\ \hat{\nu}_y^{(i)} =& \sin\hat{\gamma}^{(i)}\cos\hat{\theta}^{(i)}\sin\hat{\phi}^{(i)}e^{-j\hat{\eta}^{(i)}} + \cos\hat{\gamma}^{(i)}\cos\hat{\phi}^{(i)}. \end{aligned} \quad (20)$$

Since the above algorithm uses the ratios of cross-correlation to powers of the beamformed output signals to obtain the polarization state information and to track it adaptively, it is referred to as *cross-correlation-to-power ratio polarization tracking* (CPRPT). The joint DBT and CPRPT algorithm is summarized in Table I.

IV. Joint Adaptive AoA and Polarization Estimation for Localized Arrays

In this section, we study the estimations of AoA and polarization state using a localized array. The DBPS algorithm is proposed to remove the phase ambiguity in AoA estimation, and to determine the signal, the power of which is to be used in polarization state estimation.

For a localized array, $d_x^s = N_x d$ and $d_y^s = N_y d$. This indicates that the values for u_x (u_y) will no longer be constrained within the range of $[-\pi, \pi)$, resulting in the phase ambiguity. For the cross-correlations in (9), $\hat{R}_x^{(i)}$ ($\hat{R}_y^{(i)}$), there are $2\lfloor N_x/2 \rfloor + 1$ ($2\lfloor N_y/2 \rfloor + 1$) possible values for the estimates of u_x (u_y), given by $\hat{u}_{x,p}^{(i)} = 2\pi p + \arg\{\hat{R}_x^{(i)}\}$, $p = -\lfloor N_x/2 \rfloor, -\lfloor N_x/2 \rfloor + 1, ..., \lfloor N_x/2 \rfloor$ ($\hat{u}_{y,q}^{(i)} = 2\pi q + \arg\{\hat{R}_y^{(i)}\}$, $q = -\lfloor N_y/2 \rfloor, -\lfloor N_y/2 \rfloor + 1, ..., \lfloor N_y/2 \rfloor$), where $\lfloor \cdot \rfloor$ denotes the floor function. Therefore, a search over all the possible ps and qs is needed to identify the real AoA. Because of the alignment between the array and the incident wave, the maximum received power is produced when the real AoA is used to configure the analog and digital beamformers.

The search is conducted through receiving a sequence of reference signals which are referred to as *a scanning frame*. The frame consists of $(2\lfloor N_x/2 \rfloor + 1) \times (2\lfloor N_y/2 \rfloor + 1)$ subframes each with I_2 symbols. Each possible AoA is used to configure the analog and digital beamformers, and then tested by the reception of a subframe. $\forall (p, q)$, the phase shifters of a subarray and the weights of digital beamformers can be expressed as $\hat{\alpha}_0, ..., \hat{\alpha}_{N_x N_y - 1}$ and $\hat{\omega}_0, ..., \hat{\omega}_{M_x M_y - 1}$, respectively, where $\hat{\alpha}_{n_y N_x + n_x}^{(i)}(p, q) = -\left(\frac{n_x}{N_x} \hat{u}_{x,p}^{(i-1)} + \frac{n_y}{N_y} \hat{u}_{y,q}^{(i-1)} \right)$ and $\hat{w}_{m_y M_x + m_x}^{(i)}(p, q) = \frac{1}{M_x M_y} e^{-j(m_x \hat{u}_{x,p}^{(i)} + m_y \hat{u}_{y,q}^{(i)})}$. Thus, the outputs of the digital beamformers for x- and y-axis dipoles can be expressed as

$$[s_x[i,p,q], s_y[i,p,q]] = \frac{1}{M_x M_y} \sum_{m_y=0}^{M_y-1} \sum_{m_x=0}^{M_x-1} e^{-j(m_x \hat{u}_{x,p}^{(i)} + m_y \hat{u}_{y,q}^{(i)})} \cdot \left[s_x^{m_y M_x + m_x}[i], s_y^{m_y M_x + m_x}[i] \right]. \quad (21)$$

The resulting powers can be estimated iteratively as

$$\hat{P}_l^{(i)}(p,q) = (1-\beta)\hat{P}_l^{(i-1)}(p,q) + \beta \left(|s_l[i,p,q]|^2 - \frac{\sigma_n^2}{M_x M_y} \right), \quad (22)$$

where l denotes the subscript x or y, and $0 < \beta < 1$ is the updating coefficient, which is preferred to be inversely proportional to the length of the subframe. After the whole frame is received, the signal power estimated in the last iteration of each subframe, $\hat{P}_l^{(I_2)}(p, q)$, is used to determine the estimate of AoA, i.e.,

$$(p_{max}, q_{max}, l_{max}) = \underset{p,q,l}{\operatorname{argmax}} \left\{ \hat{P}_l^{(I_2)}(p,q) \right\}. \quad (23)$$

In fact, the search can be extended by using multiple scanning frames (See Fig. 6).

In addition to the values for p and q, (23) also reflects the powers collected by x- and y-axis dipoles for all the possible AoAs. In the absence of additive noise, identical values are expected for the estimates of polarization state given by (15) and (16). However, this does not hold in the presence of noise. The performance of estimation will depend on the relative values between the signal and noise powers in $\hat{P}_x^{(i)}$ and $\hat{P}_y^{(i)}$. The search returns the dipole that collects more signal power for CPRPT. This is because the additive noises in x- and y-axis dipoles result in identical noise powers in $\hat{P}_x^{(i)}$ and $\hat{P}_y^{(i)}$, and thus the dipole with higher signal power will have higher relative value which leads to better performance. The search procedure using one scanning frame is summarized in Table II. Once the values for p and q, and the dipole are determined, they can be used in conjunction with DBT and CPRPT for the estimations of AoA and polarization state.

TABLE II
The DBPS algorithm

Initialization: $\hat{u}_x^{(0)}$, $\hat{u}_y^{(0)}$, $\hat{R}_x^{(0)}$ and $\hat{R}_y^{(0)}$;
$\forall (p, q, l)$, $\hat{P}_l^{(0)}(p, q)$;
For $p = -\lfloor N_x/2 \rfloor : \lfloor N_x/2 \rfloor$
  For $q = -\lfloor N_y/2 \rfloor : \lfloor N_y/2 \rfloor$
    For $i = 1 : I_2$
1. Set $\hat{\alpha}_{n_y N_x + n_x}^{(i)}(p, q) = -\left[\frac{n_x}{N_x}(2\pi p + \hat{u}_x^{(i-1)}) + \frac{n_y}{N_y}(2\pi q + \hat{u}_y^{(i-1)}) \right]$, $n_x = 0, ..., N_x - 1, n_y = 0, ..., N_y - 1$;
2. Update $[s_x^m[i], s_y^m[i]]$ using $\hat{\alpha}_{n_y N_x + n_x}^{(i)}(p, q)$ in (1);
3. Update $\hat{R}_x^{(i)}$ and $\hat{R}_y^{(i)}$ using (9);
4. Calculate $\hat{u}_x^{(i)} = \arg\{\hat{R}_x^{(i)}\}$ and $\hat{u}_y^{(i)} = \arg\{\hat{R}_y^{(i)}\}$;
5. Update $\hat{w}_{m_y M_x + m_x}^{(i)}(p, q) = \frac{1}{M_x M_y} e^{-j(m_x \hat{u}_{x,p}^{(i)} + m_y \hat{u}_{y,q}^{(i)})}$, $m_x = 0, ..., M_x - 1$, $m_y = 0, ..., M_y - 1$;
6. Update $[s_x[i, p, q], s_y[i, p, q]]$ using (21);
7. Calculate $\hat{P}_l^{(i)}(p, q)$ using (22);
    End for i
  End for q
End for p
Output: $(p_{max}, q_{max}, l_{max})$ using (23).

The joint DBT and CPRPT algorithm, and DBPS algorithm are blind adaptive since no knowledge about the reference signal is required. These provide not only efficient online estimation approaches, but also the benefit of bandwidth saving and no need of specific training sequences. They are applicable to the scenarios where the system available bandwidth is limited and/or training sequences are not specified. When there exists relative motion between the transmitter and the receiver, the Doppler effect will happen and the AoA and polarization state may vary with the time. However, as shown in (6), (7) and (12), the phase shift $e^{j2\pi f_D t}$ induced by the Doppler frequency shift f_D affects neither the cross-correlations $[R_x, R_y]$, nor the cross-correlation and powers $[Q_{xy}, P_x, P_y]$, since this phase shift is the same for any beamformer output signal at any given instance. That means

f_D does not affect the instantaneous estimates of AoA and polarization. When the AoA and polarization state are time-varying, the proposed adaptive filtering based algorithms can track AoA and polarization state adaptively. As a result, the proposed algorithms are also Doppler resilient.

V. Performance of Cross-correlation-to-power Ratio Polarization Tracking

In this section, we present an analysis on the CPRPT in the context of a linear hybrid dual-polarized array with M interleaved subarrays[4] [5]. It is shown that the ratios, $\hat{Q}_{xy}^{(i)}/\hat{P}_x^{(i)}$ and $\hat{Q}_{xy}^{(i)}/\hat{P}_y^{(i)}$, converge to E_y^*/E_x^* and E_x/E_y, respectively, as the number of iterations increases. Therefore, the estimate of the polarization state obtained by CPRPT is asymptotically unbiased.

Because of the similar statistic distributions of $\hat{P}_x^{(i)}$ and $\hat{P}_y^{(i)}$, we present an elaborated derivation for the ratio, $\hat{Q}_{xy}^{(i)}/\hat{P}_x^{(i)}$, only. Eq. (10) can be rewritten as

$$[s_x[i], s_y[i]] = \frac{[E_x, E_y]}{\sqrt{|E_x|^2+|E_y|^2}}\tilde{s}[i]P_s(\Delta\hat{u}^{(i-1)})P_c(\Delta\hat{u}^{(i)}) + [\xi_x[i], \xi_y[i]], \tag{24}$$

where $P_s(\Delta\hat{u}^{(i-1)}) = \frac{\sin[MN\Delta\hat{u}^{(i-1)}/2]}{N\sin[M\Delta\hat{u}^{(i-1)}/2]}$ denotes the normalized subarray radiation pattern, with $\Delta\hat{u}^{(i-1)} = u - \hat{u}^{(i-1)}$ representing the difference between the real and estimated phases, and N, the number of elements in each subarray. For a linear array, the phase, u, is given by $u = \frac{2\pi}{\lambda}d\sin\theta$, and $P_c(\Delta\hat{u}^{(i)})$ can be rewritten as $\frac{\sin[M\Delta\hat{u}^{(i)}/2]}{M\sin[\Delta\hat{u}^{(i)}/2]}$. $[\xi_x[i], \xi_y[i]]$ are the independent complex AWGNs both with power of σ_n^2/M. Then the updates, $q_{xy}[i] = s_x[i]s_y^*[i]$ and $p_x[i] = |s_x[i]|^2 - \sigma_n^2/M$ can be expressed as

$$q_{xy}[i] = \frac{E_xE_y^*|\tilde{s}[i]|^2}{|E_x|^2+|E_y|^2}\left|P_s(\Delta\hat{u}^{(i-1)})\right|^2\left|P_c(\Delta\hat{u}^{(i)})\right|^2 + \xi_{xy}[i] \tag{25}$$

and

$$p_x[i] = \frac{|E_x|^2|\tilde{s}[i]|^2}{|E_x|^2+|E_y|^2}\left|P_s(\Delta\hat{u}^{(i-1)})\right|^2\left|P_c(\Delta\hat{u}^{(i)})\right|^2 + \xi_{xx}[i], \tag{26}$$

respectively, where

$$\xi_{xy}[i] = \frac{E_x\tilde{s}[i]P_s(\Delta\hat{u}^{(i-1)})P_c(\Delta\hat{u}^{(i)})}{\sqrt{|E_x|^2+|E_y|^2}}\xi_y^*[i] + \xi_x[i]\xi_y^*[i] + \frac{E_y^*\tilde{s}^*[i]P_s^*(\Delta\hat{u}^{(i-1)})P_c^*(\Delta\hat{u}^{(i)})}{\sqrt{|E_x|^2+|E_y|^2}}\xi_x[i] \tag{27}$$

and

$$\xi_{xx}[i] = \frac{E_x\tilde{s}[i]P_s(\Delta\hat{u}^{(i-1)})P_c(\Delta\hat{u}^{(i)})}{\sqrt{|E_x|^2+|E_y|^2}}\xi_x^*[i] + |\xi_x[i]|^2 + \frac{E_x^*\tilde{s}^*[i]P_s^*(\Delta\hat{u}^{(i-1)})P_c^*(\Delta\hat{u}^{(i)})}{\sqrt{|E_x|^2+|E_y|^2}}\xi_x[i] - \frac{\sigma_n^2}{M} \tag{28}$$

denote the noise components induced in the ith iteration. They can be approximated by complex Gaussian noises with zero means, and noise powers $|\tilde{s}[i]|^2\left|P_s(\Delta\hat{u}^{(i-1)})\right|^2\left|P_c(\Delta\hat{u}^{(i)})\right|^2\sigma_n^2/M$ for (27) and $\frac{2|E_x|^2|\tilde{s}[i]|^2}{|E_x|^2+|E_y|^2}\left|P_s(\Delta\hat{u}^{(i-1)})\right|^2\left|P_c(\Delta\hat{u}^{(i)})\right|^2\sigma_n^2/M$ for (28), respectively.

The CPRPT algorithm estimates the polarization state using the ratio, $\hat{Q}_{xy}^{(i)}/\hat{P}_x^{(i)}$, where

$$\hat{Q}_{xy}^{(i)} = \sum_{k=1}^{i}q_{xy}[k] = \frac{E_xE_y^*}{|E_x|^2+|E_y|^2}\sum_{k=1}^{i}|\tilde{s}[k]|^2\left|P_s(\Delta\hat{u}^{(k-1)})\right|^2 \cdot\left|P_c(\Delta\hat{u}^{(k)})\right|^2 + \sum_{k=1}^{i}\xi_{xy}[k] \tag{29}$$

and

$$\hat{P}_x^{(i)} = \sum_{k=1}^{i}p_x[k] = \frac{|E_x|^2}{|E_x|^2+|E_y|^2}\sum_{k=1}^{i}|\tilde{s}[k]|^2\left|P_s(\Delta\hat{u}^{(k-1)})\right|^2 \cdot\left|P_c(\Delta\hat{u}^{(k)})\right|^2 + \sum_{k=1}^{i}\xi_{xx}[k]. \tag{30}$$

Since the polarization state information is included in the terms, $\frac{E_xE_y^*}{|E_x|^2+|E_y|^2}$ and $\frac{|E_x|^2}{|E_x|^2+|E_y|^2}$, in (29) and (30), respectively, they are taken as the wanted components which are subject to scaling and additive noise. As a result, the conditional SNRs of $\hat{Q}_{xy}^{(i)}$ and $\hat{P}_x^{(i)}$, in the presence of random nuisance parameters $\tilde{s}[k]$, $k = 1, 2, ..., i$, and $\hat{u}^{(k)}$, $k = 0, 1, ..., i$, denoted by $\tilde{\mathbf{s}}$ and $\hat{\mathbf{u}}^{(i)}$ respectively, can be expressed as

$$\rho_{Q\,\tilde{\mathbf{s}},\hat{\mathbf{u}}^{(i)}}^{(i)} = \frac{\left|\sum_{k=1}^{i}|\tilde{s}[k]|^2|P_s(\Delta\hat{u}^{(k-1)})|^2|P_c(\Delta\hat{u}^{(k)})|^2\right|^2}{\sum_{k=1}^{i}|\tilde{s}[k]|^2\left|P_s(\Delta\hat{u}^{(k-1)})\right|^2\left|P_c(\Delta\hat{u}^{(k)})\right|^2\sigma_n^2/M} = \frac{M}{\sigma_n^2}\sum_{k=1}^{i}|\tilde{s}[k]|^2\left|P_s(\Delta\hat{u}^{(k-1)})\right|^2\left|P_c(\Delta\hat{u}^{(k)})\right|^2 \tag{31}$$

and

$$\rho_{P\,\tilde{\mathbf{s}},\hat{\mathbf{u}}^{(i)}}^{(i)} = \frac{1}{2}\left(1+\frac{|E_y|^2}{|E_x|^2}\right)\rho_{Q\,\tilde{\mathbf{s}},\hat{\mathbf{u}}^{(i)}}^{(i)}, \tag{32}$$

respectively. As shown in (31) and (32), the SNRs increase with increasing number of iterations. For a value for i great enough, both $P_s(\Delta\hat{u}^{(i-1)})$ and $P_c(\Delta\hat{u}^{(i)})$ approach to ones, indicating that $|\tilde{s}[i]|^2\left|P_s(\Delta\hat{u}^{(i-1)})\right|^2\left|P_c(\Delta\hat{u}^{(i)})\right|^2$ does not approach to zero. Therefore, as i approaches to ∞, both the SNRs also approach to ∞, implying that the noise components in (29) and (30) gradually become negligible as the iteration proceeds. As a result, the noise components can be omitted after a sufficient number of iterations, leading to the ratio, $\hat{Q}_{xy}^{(i)}/\hat{P}_x^{(i)}$, converging to E_y^*/E_x^*. Therefore, the estimator

[4]The performance of AoA estimation has been studied in the previous research in the context of a linear array with one-directional dipole antennas [18]. The methods used in [18] can be directly extended for the dual-polarized arrays. Thus, the analysis for AoA estimation is omitted in this paper, but the resulting MSEs are presented in the simulation results.

[5]As shown in (3) and (11), both $P_s(\theta,\phi)$ and $P_c(u_x,u_y)$ are the products of the corresponding patterns along x- and y-directions, respectively. These two directional patterns are independent and can be decoupled from each other. Therefore, the result for the planar array is a direct extension of the linear array. To simplify the analysis, we consider a linear array here.

based on the ratio is asymptotically unbiased.

The evaluation of the resulting MSE requires the exact form of probability density function (pdf) of the ratio, $\hat{Q}_{xy}^{(i)}/\hat{P}_x^{(i)}$. However, as far as we know, its closed form is unknown as the pdf of the ratio of two correlated complex Gaussian random variables with non-zero means is not available. Therefore, instead of providing the MSE, the upper bounds of the average SNRs of $\hat{Q}_{xy}^{(i)}$ and $\hat{P}_x^{(i)}$ are derived to indirectly illustrate the accuracy of CPRPT as the estimation proceeds. Taking the expectations of $\rho_{Q\ \tilde{\mathbf{s}},\hat{\mathbf{u}}^{(i)}}^{(i)}$ and $\rho_{P\ \tilde{\mathbf{s}},\hat{\mathbf{u}}^{(i)}}^{(i)}$ on $\tilde{\mathbf{s}}$ and $\hat{\mathbf{u}}^{(i)}$, respectively, one can obtain the corresponding average SNRs at the ith iteration as $\bar{\rho}_Q^{(i)}$ and $\bar{\rho}_P^{(i)}$, which are upper bounded by (See Appendix B)

$$UB(\bar{\rho}_Q^{(i)}) = \frac{\rho}{2\pi MN^2}\sum_{k=1}^{i}\int_{-\pi}^{\pi}\frac{\sin^2(MN\hat{u}^{(k)}/2)}{\sin^2(\hat{u}^{(k)}/2)} \cdot\frac{\sqrt{\bar{\rho}_s^{(k)}\pi^2+1}}{\left[\bar{\rho}_s^{(k)}(\hat{u}^{(k)})^2+1\right]^{3/2}}d\hat{u}^{(k)} \tag{33}$$

and $UB(\bar{\rho}_P^{(i)}) = \frac{1}{2}\left(1+|E_y|^2/|E_x|^2\right)\cdot UB(\bar{\rho}_Q^{(i)})$, respectively, where $\rho = \sigma_{\tilde{s}}^2/\sigma_n^2$, and $\bar{\rho}_s^{(i)}$ is the average SNR of $\hat{R}^{(i)}$, which is recursively determined as

$$\bar{\rho}_s^{(i)} = \begin{cases} \frac{(M-1)\rho}{2N}, & i=1 \\ \bar{\rho}_s^{(i-1)} + \frac{(M-1)\rho}{4\pi N^2}\int_{-\pi}^{\pi}\frac{\sin^2(MN\hat{u}^{(i-1)}/2)}{\sin^2(M\hat{u}^{(i-1)}/2)} \\ \cdot\frac{\sqrt{\bar{\rho}_s^{(i-1)}\pi^2+1}}{\left[\bar{\rho}_s^{(i-1)}(\hat{u}^{(i-1)})^2+1\right]^{3/2}}d\hat{u}^{(i-1)}. & i>1 \end{cases} \tag{34}$$

VI. Numerical and Simulation Results

In this section, we present the numerical and simulation results to demonstrate the performance of the proposed array. The planar arrays with interleaved and localized subarrays are studied, where the arrays are divided into two subarrays in both x- and y-directions, respectively, i.e., $M_x = M_y = 2$. Each subarray consists of four antenna elements in both x- and y-directions respectively, with the spacing between the neighbouring elements given by half of the wavelength of the incident wave, i.e., $N_x = N_y = 4$ and $d = \lambda/2$. Unless otherwise specified, we consider the reception of an elliptically-polarized wave with the polarization state and AoA given by $\gamma = \pi/4 = 0.7854$, $\eta = -\pi/4 = -0.7854$, $\theta = \pi/4$ and $\phi = 0$. These correspond to $u_x = \sqrt{2}\pi/2 = 2.2214$ and $u_y = 0$ for the interleaved array, and $u_x = 2\sqrt{2}\pi = 8.8858$ and $u_y = 0$ for the localized array, respectively. The ratio of the received signal power on x-axis dipoles to that on y-axis dipoles is 0.5, i.e., $|E_x|^2/|E_y|^2 = 0.5$. Note that circular and linear polarization can be considered to be special cases of elliptical polarization. Although a state-determined elliptically-polarized wave is used in the simulation, the proposed algorithms are still applicable to circularly or linearly-polarized wave. We assume that the reference signal, $\tilde{s}(t)$, is a complex Gaussian process due to the absence of synchronization between the transceivers, and denote the equivalent average SNR per antenna element by ρ_a which is given by $\rho_a = \rho/(N_xN_y)$.

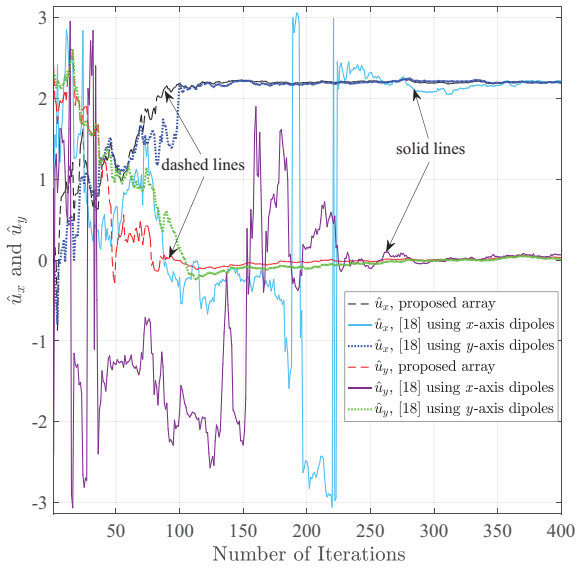

Fig. 3. $\hat{u}_x$ and $\hat{u}_y$ using DBT for interleaved arrays.

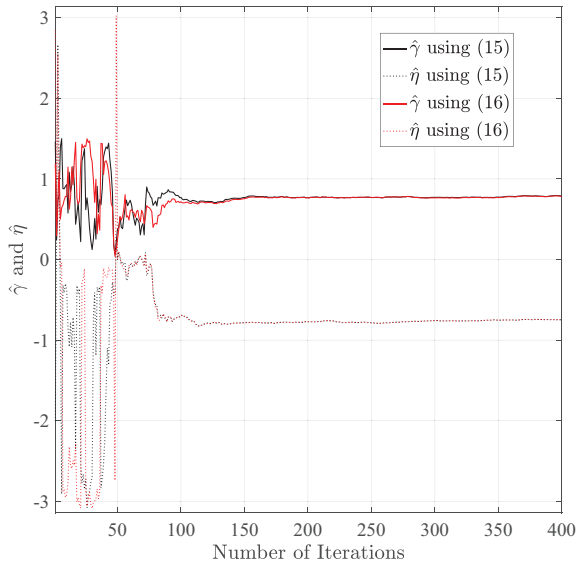

Fig. 4. $\hat{\gamma}$ and $\hat{\eta}$ using CPRPT for interleaved arrays.

The updating coefficients, μ_a, μ_p and β, are set to 0.01, 0.001 and 0.25 respectively in the simulation.

The simulation results using joint DBT and CPRPT for interleaved arrays versus the number of iterations are shown in Figs. 3-5, where an SNR per element of -5dB is assumed. Fig. 3 shows some realizations of the estimated AoA information. As a comparison, the AoA estimations using a conventional array [18] (using only x- or y-axis dipoles) with the same number of antennas are also plotted. It is seen that the proposed array (dashed lines) outperforms the conventional ones (solid and dotted lines) in terms of the speed of convergence and fluctuation variance. The estimation of polarization state information is shown in Fig. 4. As shown in the figure, both the estimates, $\hat{\gamma}$ and $\hat{\eta}$ based on $\hat{Q}_{xy}^{(i)}/\hat{P}_x^{(i)}$ and $\hat{Q}_{xy}^{(i)}/\hat{P}_y^{(i)}$, respectively, converge to the real polarization state with increasing number of iterations. The results obtained after 400 iterations are given by $\{0.7894, -0.7494\}$ and $\{0.7841, -0.7494\}$, respectively.

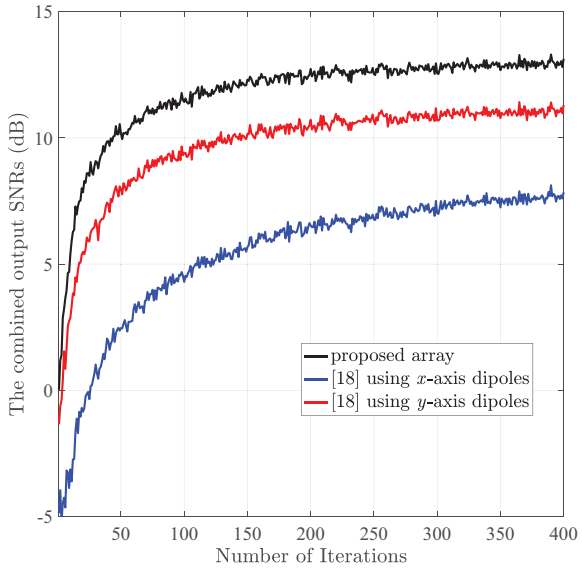

Fig. 5. The combined output SNRs using joint DBT and CPRPT for interleaved arrays.

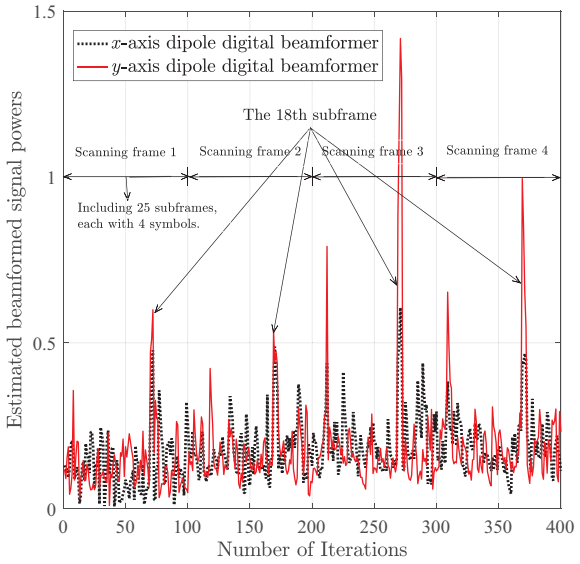

Fig. 6. Estimated beamformed signal power profile for all the possible AoAs.

Fig. 5 shows the SNRs of the combined signal using the proposed array, and of the signals using a conventional array using x- or y-axis dipoles only. Here, the SNR of the combined signal is defined as the output SNR of $s[i]$ in (5) with MRC. The results are obtained by averaging 1000 independent simulations. It is seen that the coherent combination in the proposed array produces the highest output SNR compared with those by the conventional array with one-directional dipoles. Since the accuracy of estimated AoA and polarization state improves with increasing number of iterations, the resulting SNRs increase accordingly. Note that the simulated output SNRs using the proposed and conventional arrays after 400 iterations are given by 13.04dB, 7.72dB (x-axis dipoles) and 11.19dB (y-axis dipoles), respectively. These are close to the SNRs that are achieved by the arrays perfectly aligned with the real AoA and polarization state, given by $-5+10\log(4\times 16)=13$dB, $13+10\log(1/3)=8.23$dB and $13+10\log(2/3)=11.24$dB, respectively.

The simulation results using DBPS for localized arrays are shown in Fig. 6, where the SNR per antenna element is configured at -9dB. The signal powers collected from x- and y-axis dipoles for all the possible AoAs are demonstrated through the reception of four scanning frames, each consisting of 100 symbols. Given the AoAs and $N_x = N_y = 4$, the possible values for u_x are given by $2(\sqrt{2}-3)\pi$, $2(\sqrt{2}-2)\pi$, $2(\sqrt{2}-1)\pi$, $2\sqrt{2}\pi$ and $2(\sqrt{2}+1)\pi$, and those for u_y, by -4π, -2π, 0, 2π and 4π. Therefore, there are 25 possible AoA combinations that need to be searched over one frame, leading to four symbols included in each subframe. From Fig. 6, it can be seen that the indexes of the subframes which can achieve the maximum powers in all the four frames are identical given by 18. It corresponds to the beam with the fourth value of $u_x = 2\sqrt{2}\pi$ and the third value of $u_y = 0$. As a result, the corresponding AoAs are determined as the estimates which match the real AoAs. We can also see that y-axis dipoles can collect more power than x-axis dipoles because of the polarization state of the wave. Therefore, the power $\hat{P}_y^{(i)}$ will be used in CPRPT.

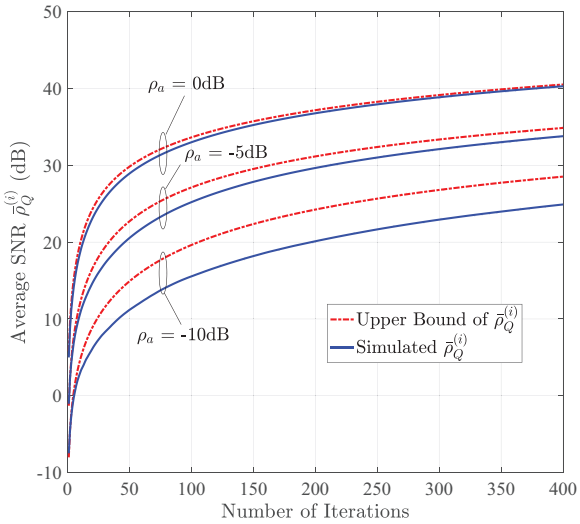

Fig. 7. Simulated $\bar{\rho}_Q^{(i)}$ and its corresponding upper bounds.

The upper bound of $\bar{\rho}_Q^{(i)}$, $UB(\bar{\rho}_Q^{(i)})$, is verified in Fig. 7 for $\rho_a = -10, -5$ and 0dB, respectively. A linear hybrid array with four interleaved subarrays each consisting of eight elements is considered. We assume that the reference signal has a fixed AoA, $\theta = \pi/4$ and polarization state, $\gamma = \pi/4$ and $\eta = -\pi/4$. As shown in the figure, the upper bound is relatively loose for low SNRs per antenna element, but becomes tight as the SNR increases. It can be seen that the bound almost matches the simulated values for an SNR of 0dB. From the figure, we can also see that the simulated average SNR, $\bar{\rho}^{(i)}$, increases as the iteration proceeds, but its rate of increase gradually drops. This is confirmed by (45) which shows that the ratio, $\bar{\rho}_Q^{(i+1)}/\bar{\rho}_Q^{(i)}$, can be approximated by $1+1/\bar{\rho}_Q^{(i)}$ for a sufficiently large i. In this case, $\mathbb{E}\left\{\left|P_s(\Delta\hat{u}^{(i)})\right|^2\left|P_c(\Delta\hat{u}^{(i)})\right|^2\right\}$ is close to one as the difference of phase, $\Delta\hat{u}^{(i)}$, approximately equals zero.

Figs. 8 and 9 show the simulated MSEs achieved by the proposed array and algorithm, where the results for AoA are

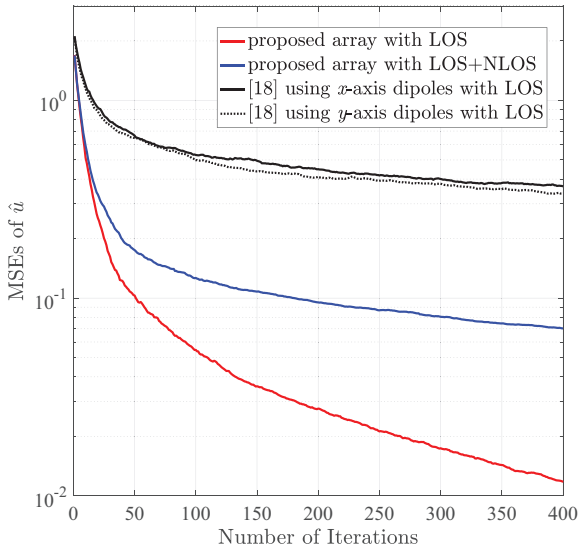

Fig. 8. Simulated MSEs of $\hat{u}$ versus the number of iterations.

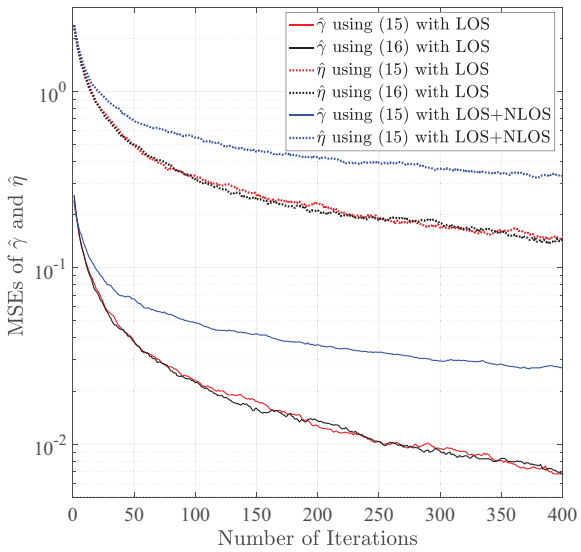

Fig. 9. Simulated MSEs of $\hat{\gamma}$ and $\hat{\eta}$ versus the number of iterations.

plotted in Fig. 8 and those for polarization state in Fig. 9. The received signal is assumed to experience a LOS path with $\rho_a = 0$dB and a NLOS path with $\rho_a = -10$dB. For AoA estimation, the real values of AoAs in the LOS path and NLOS path, u and u_N, are assumed to follow uniform distribution within $[\pi/6, \pi/3]$ and $[-\pi/3, -\pi/6]$, respectively. For polarization estimation, γ and η, are uniformly distributed over $[0, \frac{\pi}{2}]$ and $[-\pi, \pi]$, respectively. The results are obtained by averaging 10,000 independent simulations in an array identical to that for Fig. 7. For comparison, the MSEs achieved by *x*-/*y*-axis dipoles only are also plotted in Fig. 8. It can be seen from Fig. 8 that the proposed array and algorithm outperform its conventional counterparts in estimating the AoA. After 400 iterations, the proposed array can achieve an MSE of 0.012, whereas the conventional array using *x*-axis dipoles only, 0.367. We can also see that compared with the case of LOS only, the presence of a NLOS path leads to a degradation in AoA estimation. This is because the NLOS component leads to signal-dependent interference in the cross-correlations given by (6) and (7), resulting in the estimated AoA deviating away from the LOS. It can be seen from Fig. 9 that the MSEs of polarization state estimated by using (15) and (16) decrease with the number of iterations. This is in line with the analysis of the CPRPT estimator where the SNRs of the nominator and denominator improve as the iteration proceeds. Due to the randomness of the real AoA and polarization state, the curves evaluated by using (15) is observed to have similar performance to those by using (16). In addition, similar with AoA estimation, the accuracy of polarization estimation degrades when a NLOS path is present.

VII. Conclusion

In this paper, we have proposed a hybrid dual-polarized adaptive antenna array, which not only significantly lowers full digital implementation complexity, but also makes use of polarization diversity to greatly enhance the capacity and reliability of mmWave communication systems. For the interleaved and localized configurations, we develop a joint DBT and CPRPT algorithm, and a DBPS algorithm respectively, which are blind adaptive and Doppler resilient. The former is applicable for tracking fast time-varying AoA and polarization state due to its high estimation convergence speed. The latter is suitable in the AoA and polarization acquisition stage due to the ambiguity caused by the localized array. Furthermore, we have formulated the polarization state estimation as the ratio estimation of cross-correlation to powers of two beamformed signals under recursive nuisance parameters, and proved the CPRPT estimator to be asymptotically unbiased. Numerical and simulation results show that the proposed algorithms can be efficiently and effectively performed for AoA and polarization state estimations with a large hybrid dual-polarized antenna array of subarrays.

Appendix A
The Derivation of (γ, η) Estimation

From (13), we have

$$\begin{aligned} U_x + jV_x =& \frac{\sin\gamma\cos\theta\sin\phi e^{-j\eta} + \cos\gamma\cos\phi}{\sin\gamma\cos\theta\cos\phi e^{-j\eta} - \cos\gamma\sin\phi} \\ \overset{(a)}{=}& \frac{\tan\phi\cdot x^2 + \cos\eta(1-\tan^2\phi)x - \tan\phi}{x^2 - 2\cos\eta\tan\phi\cdot x + \tan^2\phi} \\ &+ \frac{j\sin\eta(1+\tan^2\phi)x}{x^2 - 2\cos\eta\tan\phi\cdot x + \tan^2\phi}, \end{aligned} \tag{35}$$

where (a) holds assuming $x = \tan\gamma\cos\theta > 0$. From the equality between the real parts (and the imaginary parts) of two sides of (35), respectively, we can derive

$$\begin{aligned} \sin\eta =& \frac{V_x(x^2 - \tan^2\phi)}{(1 + 2U_x\tan\phi - \tan^2\phi)x} \\ \cos\eta =& \frac{(U_x - \tan\phi)x^2 + \tan\phi(U_x\tan\phi + 1)}{(1 + 2U_x\tan\phi - \tan^2\phi)x}. \end{aligned} \tag{36}$$

According to $\sin^2\eta + \cos^2\eta = 1$, the unknown variable x can be obtained as

$$x = \tan\gamma\cos\theta = \sqrt{\frac{(U_x\tan\phi + 1)^2 + V_x^2\tan^2\phi}{(U_x - \tan\phi)^2 + V_x^2}}. \tag{37}$$

As a result, (15) is derived based on (37) and (36). Similarly, (16) is derived.

APPENDIX B
RECURSIVE UPPER BOUNDS OF $\bar{\rho}_Q^{(i)}$ AND $\bar{\rho}_P^{(i)}$

From (32), we have $\bar{\rho}_P^{(i)} = \frac{1}{2}\left(1+|E_y|^2/|E_x|^2\right)\bar{\rho}_Q^{(i)}$, resulting in $UB(\bar{\rho}_P^{(i)}) = \frac{1}{2}\left(1+|E_y|^2/|E_x|^2\right)\cdot UB(\bar{\rho}_Q^{(i)})$. As a result, we only derive $UB(\bar{\rho}_Q^{(i)})$ in the following. Firstly, we derive (34). The differential signal between $s_x^m[i]$ and $s_x^{m+1}[i]$ is

$$\begin{aligned} r_x^m[i] =&(s_x^m[i])^* s_x^{m+1}[i] \\ =&\frac{|E_x|^2|\tilde{s}[i]|^2}{|E_x|^2+|E_y|^2}|P_s(\Delta\hat{u}^{(i-1)})|^2 e^{ju} + (\xi_x^m[i])^*\xi_x^{m+1}[i] \\ &+\frac{E_x\tilde{s}[i]}{\sqrt{|E_x|^2+|E_y|^2}}P_s(\Delta\hat{u}^{(i-1)})e^{j(m+1)u}(\xi_x^m[i])^* \\ &+\frac{E_x^*\tilde{s}^*[i]}{\sqrt{|E_x|^2+|E_y|^2}}P_s^*(\Delta\hat{u}^{(i-1)})e^{-jmu}\xi_x^{m+1}[i] \\ =&\frac{|E_x|^2|\tilde{s}[i]|^2}{|E_x|^2+|E_y|^2}|P_s(\Delta\hat{u}^{(i-1)})|^2 e^{ju} + z_x^m[i]. \end{aligned} \tag{38}$$

Equally, the differential signal $r_y^m[i]$ on the y-axis dipoles is

$$r_y^m[i] = \frac{|E_y|^2|\tilde{s}[i]|^2}{|E_x|^2+|E_y|^2}|P_s(\Delta\hat{u}^{(i-1)})|^2 e^{ju} + z_y^m[i]. \tag{39}$$

In (38) and (39), $z_x^m[i]$ and $z_y^m[i]$ can be approximated as complex Gaussian noises with zero means and total noise powers $\frac{2|E_x|^2|\tilde{s}[i]|^2}{|E_x|^2+|E_y|^2}|P_s(\Delta\hat{u}^{(i-1)})|^2\sigma_n^2$ and $\frac{2|E_y|^2|\tilde{s}[i]|^2}{|E_x|^2+|E_y|^2}|P_s(\Delta\hat{u}^{(i-1)})|^2\sigma_n^2$, respectively.

According to the DBT algorithm, $\hat{u}^{(i)}$ is obtained by

$$\hat{u}^{(i)} = \arg\left\{\hat{R}^{(i)}\right\} = \arg\left\{\sum_{k=1}^{i}\sum_{m=0}^{M-2}(r_x^m[k]+r_y^m[k])\right\}, \tag{40}$$

where $\hat{R}^{(i)}$ follows complex Gaussian distribution with the conditional mean and variance [18]

$$\begin{aligned} m_{\hat{R}^{(i)}} =&(M-1)\sum_{k=1}^{i}|\tilde{s}[k]|^2|P_s(\Delta\hat{u}^{(k-1)})|^2 e^{ju} \\ \sigma^2_{\hat{R}^{(i)}} =&2(M-1)\sum_{k=1}^{i}|\tilde{s}[k]|^2|P_s(\Delta\hat{u}^{(k-1)})|^2\sigma_n^2. \end{aligned}$$

Thus, the conditional SNR of $\hat{R}^{(i)}$, $\rho_{s\,\tilde{\mathbf{s}},\hat{\mathbf{u}}^{(i-1)}}^{(i)}$, is given by

$$\rho_{s\,\tilde{\mathbf{s}},\hat{\mathbf{u}}^{(i-1)}}^{(i)} = \frac{|m_{\hat{R}^{(i)}}|^2}{\sigma^2_{\hat{R}^{(i)}}} = \frac{M-1}{2\sigma_n^2}\sum_{k=1}^{i}|\tilde{s}[k]|^2|P_s(\Delta\hat{u}^{(k-1)})|^2.$$

Taking the expectation of $\rho_{s\,\tilde{\mathbf{s}},\hat{\mathbf{u}}^{(i-1)}}^{(i)}$ over $\tilde{\mathbf{s}}, \hat{\mathbf{u}}^{(i-1)}$, we have the average SNR of $\hat{R}^{(i)}$, $\bar{\rho}_s^{(i)}$, as

$$\begin{aligned} \bar{\rho}_s^{(i)} =&\mathbb{E}_{\tilde{\mathbf{s}},\hat{\mathbf{u}}^{(i-1)}}\left\{\rho_{s\,\tilde{\mathbf{s}},\hat{\mathbf{u}}^{(i-1)}}^{(i)}\right\} \\ =&\frac{(M-1)\rho}{2}\sum_{k=1}^{i}\mathbb{E}\left\{|P_s(\Delta\hat{u}^{(k-1)})|^2\right\}. \end{aligned} \tag{41}$$

From (41) and using the assumption that $P_s(\Delta\hat{u})$ is a periodic function [28], $\bar{\rho}_s^{(1)}$ can be determined as

$$\begin{aligned} \bar{\rho}_s^{(1)} =&\frac{(M-1)\rho}{2}\cdot\mathbb{E}\left\{|P_s(\Delta\hat{u}^{(0)})|^2\right\} \\ =&\frac{(M-1)\rho}{4\pi}\int_{-\pi}^{\pi}\frac{\sin^2(MN\hat{u}^{(0)}/2)}{N^2\sin^2(M\hat{u}^{(0)}/2)}d\hat{u}^{(0)} = \frac{(M-1)\rho}{2N}, \end{aligned} \tag{42}$$

where the initial $\hat{u}^{(0)}$ is assumed to be uniformly distributed in $[-\pi,\pi)$. $\bar{\rho}_s^{(i)}$ for $i>1$ can be recursively determined as

$$\begin{aligned} \bar{\rho}_s^{(i)} =&\frac{(M-1)\rho}{2}\sum_{k=1}^{i-1}\mathbb{E}\left\{|P_s(\Delta\hat{u}^{(k-1)})|^2\right\} \\ &+\frac{(M-1)\rho}{2}\int_{-\pi}^{\pi}|P_s(\hat{u}^{(i-1)})|^2 p_{\hat{u}^{(i-1)}}(\hat{u}^{(i-1)})d\hat{u}^{(i-1)}, \end{aligned} \tag{43}$$

where $p_{\hat{u}^{(i-1)}}(\hat{u}^{(i-1)})$ is the pdf of $\hat{u}^{(i-1)}$. Because the proposed algorithms are blind and do not require any signal synchronization, $\tilde{s}[i]$ is generally assumed to be complex Gaussian distributed, and thus $|\tilde{s}[i]|$ is Rayleigh distributed. In high SNR regions of Rayleigh fading channels, the known pdf of $\hat{u}^{(i)}$, $p_{\hat{u}^{(i)}}(\hat{u}^{(i)}) = p_1(\hat{u}^{(i)},\bar{\rho}_s^{(i)})$ [18], where

$$p_1(\hat{u}^{(i)},\bar{\rho}_s^{(i)}) \approx \frac{\sqrt{\bar{\rho}_s^{(i)}\pi^2+1}}{2\pi\left[\bar{\rho}_s^{(i)}(\hat{u}^{(i)})^2+1\right]^{3/2}}, -\pi\le\hat{u}^{(i)}<\pi. \tag{44}$$

Based on (42)-(44), (34) can be derived.

Secondly, $\bar{\rho}_Q^{(i)}$ can be represented by

$$\begin{aligned} \bar{\rho}_Q^{(i)} =&\mathbb{E}_{\tilde{\mathbf{s}},\hat{\mathbf{u}}^{(i)}}\left\{\rho_{Q\,\tilde{\mathbf{s}},\hat{\mathbf{u}}^{(i)}}^{(i)}\right\} \\ =&M\sum_{k=1}^{i}\mathbb{E}\left\{\frac{|\tilde{s}[k]|^2}{\sigma_n^2}\right\}\mathbb{E}\left\{\left|P_s(\Delta\hat{u}^{(k-1)})\right|^2\left|P_c(\Delta\hat{u}^{(k)})\right|^2\right\} \\ \approx&M\rho\sum_{k=1}^{i}\mathbb{E}\left\{\left|P_s(\Delta\hat{u}^{(k)})\right|^2\left|P_c(\Delta\hat{u}^{(k)})\right|^2\right\}. \end{aligned} \tag{45}$$

With a Gaussian distributed reference signal, if $P_s(\Delta\hat{u}) = 1$, $p_1(\hat{u}^{(i)},\bar{\rho}_s^{(i)})$ will be the true pdf of $\hat{u}^{(i)}$ in Rayleigh fading channel. However, since $|P_s(\Delta\hat{u})|\le 1$ throughout the iterative process, which will cause an SNR reduction, $\mathbb{E}\left\{\left|P_s(\Delta\hat{u}^{(k)})\right|^2\left|P_c(\Delta\hat{u}^{(k)})\right|^2\right\}$ in (45) will be always less than that calculated using $p_1(\hat{u}^{(i)},\bar{\rho}_s^{(i)})$, i.e.,

$$\begin{aligned} &\mathbb{E}\left\{\left|P_s(\Delta\hat{u}^{(k)})\right|^2\left|P_c(\Delta\hat{u}^{(k)})\right|^2\right\} \\ \le&\int_{-\pi}^{\pi}\frac{\sin^2\left(\frac{MN\hat{u}^{(k)}}{2}\right)}{N^2\sin^2\left(\frac{M\hat{u}^{(k)}}{2}\right)}\cdot\frac{\sin^2\left(\frac{M\hat{u}^{(k)}}{2}\right)}{M^2\sin^2\left(\frac{\hat{u}^{(k)}}{2}\right)}p_1(\hat{u}^{(k)},\bar{\rho}_s^{(k)})d\hat{u}^{(k)} \\ =&\frac{1}{2\pi M^2N^2}\int_{-\pi}^{\pi}\frac{\sin^2\left(\frac{MN\hat{u}^{(k)}}{2}\right)}{\sin^2\left(\frac{\hat{u}^{(k)}}{2}\right)}\cdot\frac{\sqrt{\bar{\rho}_s^{(k)}\pi^2+1}}{\left[\bar{\rho}_s^{(k)}(\hat{u}^{(k)})^2+1\right]^{3/2}}d\hat{u}^{(k)}. \end{aligned} \tag{46}$$

Substituing (46) into (45), (33) is proved.

REFERENCES

[1] V. Dyadyuk et al., "Adaptive antenna arrays for ad-hoc millimetre-wave wireless communications," M. Khatib, Ed. *Advanced Trends in Wireless Communications*, Ch. 6, InTech, pp. 93-116, Feb. 2011.

[2] S. Mumtaz, J. Rodriguez, and L. Dai, *mmWave Massive MIMO: A Paradigm for 5G*. New York, NY, USA: Academic, 2016.

[3] R. W. Heath, Jr., N. Gonzalez-Prelcic, S. Rangan, W. Roh, and A. M. Sayeed, "An overview of signal processing techniques for millimeter wave MIMO systems," *IEEE J. Sel. Topics Signal Process.*, vol. 10, no. 3, pp. 436-453, Apr. 2016.

[4] F. Sohrabi and W. Yu, "Hybrid digital and analog beamforming design for large-scale antenna arrays," *IEEE J. Sel. Topics Signal Process.*, vol. 10, no. 3, pp. 501-513, Apr. 2016.

[5] J. Zhang, X. Huang, V. Dyadyuk, and Y. Guo, "Massive hybrid antenna array for millimeter-wave cellular communications," *IEEE Wireless Commun.*, vol. 22, no. 1, pp. 79-87, Feb. 2015.

[6] X. Gao, L. Dai, S. Han, C.-L. I, and R. W. Heath, Jr., "Energy-efficient hybrid analog and digital precoding for mmWave MIMO systems with large antenna arrays," *IEEE J. Sel. Areas Commun.*, vol. 34, no. 4, pp. 998-1009, Apr. 2016.

[7] S. X. Ta, I. Park, and R. W. Ziolkowski, "Crossed dipole antennas: A review," *IEEE Antennas Propag. Mag.*, vol. 57, no. 5, pp. 107-122, Oct. 2015.

[8] C. Ding, H. Sun, R. W. Ziolkowski, and Y. J. Guo, "Simplified tightly-coupled cross-dipole arrangement for base station applications," *IEEE Access*, vol. 5, 2017, pp. 27491-27503.

[9] A. Alieldin, Y. Huang, S. J. Boyes, M. Stanley, S. D. Joseph, Q. Hua, and D. Lei, "A triple-band dual-polarized indoor base station antenna for 2G, 3G, 4G and sub-6 GHz 5G applications," *IEEE Access*, vol. 6, 2018, pp. 49209-49216.

[10] J. Song, J. Choi, S. G. Larew, D. J. Love, T. A. Thomas, and A. Ghosh, "Adaptive millimeter wave beam alignment for dual-polarized MIMO systems," *IEEE Trans. Wireless Commun.*, vol. 14, no. 11, pp. 6283-6296, Nov. 2015.

[11] O. Jo, J.-J. Kim, J. Yoon, D. Choi, and W. Hong, "Exploitation of dual-polarization diversity for 5G millimeter-wave MIMO beamforming systems," *IEEE Trans. Antennas Propag.*, vol. 65, no. 12, pp. 6646-6655, Dec. 2017.

[12] A. Alkhateeb, O. El Ayach, G. Leus, and R. W. Heath, "Channel estimation and hybrid precoding for millimeter wave cellular systems," *IEEE J. Sel. Topics Signal Process.*, vol. 8, no. 5, pp. 831-846, Oct. 2014.

[13] S.-F. Chuang, W.-R. Wu, and Y.-T. Liu, "High-resolution AoA estimation for hybrid antenna arrays," *IEEE Trans. Antennas Propag.*, vol. 63, no. 7, pp. 2955-2968, Jul. 2015.

[14] P. Stoica and A. Nehorai, "MUSIC, maximum likelihood, and Cramer-Rao bound," *IEEE Trans. Acoustics, Speech, Signal Process.*, vol. 37, no. 5, pp. 720-741, May 1989.

[15] R. Roy and T. Kailath, "ESPRIT-Estimation of signal parameters via rotational invariance techniques," *IEEE Trans. Acoust. Speech Signal Process.*, vol. 37, no. 7, pp. 984-995, Jul. 1989.

[16] Z. Xiao, T. He, P. Xia, and X. Xia, "Hierarchical codebook design for beamforming training in millimeter-wave communication," *IEEE Trans. Wireless Commun.*, vol. 15, no. 5, pp. 3380-3392, May 2016.

[17] Z. Xiao, H. Dong, L. Bai, P. Xia, and X. Xia, "Enhanced channel estimation and codebook design for millimeter-wave communication,"*IEEE Trans. Veh. Technol.*, vol. 67, no. 10, pp. 9393-9405, Oct. 2018.

[18] X. Huang, Y. J. Guo, and J. Bunton, "A hybrid adaptive antenna array," *IEEE Trans. Wireless Commun.*, vol. 9, no. 5, pp. 1770-1779, May 2010.

[19] X. Huang and Y. J. Guo, "Frequency-domain AoA estimation and beamforming with wideband hybrid arrays," *IEEE Trans. Wireless Commun.*, vol. 10, no. 8, pp. 2543-2553, Aug. 2011.

[20] J. A. Zhang, W. Ni, P. Cheng, and Y. Lu, "Angle-of-arrival estimation using different phase shifts across subarrays in localized hybrid arrays," *IEEE Commun. Lett.*, vol. 20, no. 11, pp. 2205-2208, Nov. 2016.

[21] K. Wu, W. Ni, T. Su, R. Liu, and Y. J. Guo, "Robust unambiguous estimation of angle-of-arrival in hybrid array with localized analog subarrays," *IEEE Trans. Wireless Commun.*, vol. 17, no. 5, pp. 2987-3002, May 2018.

[22] K. Wu, W. Ni, T. Su, R. Liu, and Y. J. Guo, "Fast and accurate estimation of angle-of-arrival for satellite-borne wideband communication system," *IEEE J. Sel. Areas Commun.*, vol. 36, no. 2, pp. 314-326, Feb. 2018.

[23] J. Li and R. T. Compton, "Angle and polarization estimation using ESPRIT with a polarization sensitive array," *IEEE Trans. Antennas Propag.*, vol. 39, no. 9, pp. 1376-1383, Sep. 1991.

[24] J. Li, "On polarization estimation using a crossed-dipole array," *IEEE Trans. Signal Process.*, vol. 42, no. 4, pp. 977-980, Apr. 1994.

[25] J. Li and R. T. Compton, "Two-dimensional angle and polarization estimation using the ESPRIT algorithm," *IEEE Trans. Antennas Propag.*, vol. 40, no. 5, pp. 550-555, May 1992.

[26] H. Li, T. Q. Wang, X. Huang, and Y. J. Guo, "Adaptive AoA and polarization estimation for receiving polarized mmWave signals," *IEEE Wireless Commun. Lett.*, vol. 8, no. 2, pp. 540-543, Apr. 2019.

[27] K. T. Wong and M. D. Zoltowski, "Uni-vector-sensor ESPRIT for multisource azimuth, elevation, and polarization estimation," *IEEE Trans. Antennas Propag.*, vol. 45, no. 10, pp. 1467-1474, Oct. 1997.

[28] X. Huang and Y. Jay Guo, "MSE bounds for phase estimation in presence of recursive nuisance parameters," in *IEEE Global Commun. Conf. (GLOBECOM)*, Dec. 2009.